Development of Capabilities for Cavitation Tunnel Investigation of Transitional Flows about Underwater Bodies

D. B. Clarke[1], P .A. Brandner[2] and G. J. Walker[3]

[1]Maritime Platforms Division, Defence Science and Technology Organisation, Australia
[2]Faculty of Maritime Transport and Engineering, Australian Maritime College, Australia
[3]School of Engineering, University of Tasmania, Australia

ABSTRACT
This paper provides an overview of the equipment developed and the techniques implemented so boundary layer behaviour may be examined within the Australian Maritime College Cavitation Tunnel. This work was conducted as part of a larger project to understand the flow about Unmanned Underwater Vehicles. A summary of some results for flow about a prolate spheroid is provided and discussed. These tests for the spheroid were conducted at Reynolds Numbers of 1×10^6 to 4×10^6.

INTRODUCTION
Unmanned Underwater Vehicles (UUVs) used for mine hunting and surveillance are required to operate over a large range of Reynolds numbers. When transiting to a region of interest or surveying a region they may be required to move quickly. Conversely detailed investigation of an object requires low speed manoeuverability. These UUVs operate for at least part of the time at Reynolds Numbers where laminar boundary layers may occupy a significant portion of the body surface. Attempting to model the fluid flow around these vehicles using standard implementation of a Reynolds Averaged Navier-Stokes (RANS) turbulence model is likely to result in inaccurate prediction of body forces and flow structures if the transition of the flow is ignored.
This paper details the equipment and methodology used to measure the state of the boundary layer on a 3-1 prolate spheroid.

EXPERIMENTAL DEVELOPMENT
The equipment developed to enable these experiments includes a 3D traversing system, a fast response pressure probe and the 3-1 prolate spheroid model. In addition methods were implemented to enable both accurate determination of the model position and examination of boundary layer state. The tests were performed in the Australian Maritime College (AMC) Tom Fink Cavitation Tunnel. This is a closed circuit facility with a test section of 0.6 m × 0.6 m × 2.6 m, a maximum velocity of 12 ms^{-1}, a pressure range of 4 to 400 kPa and a freestream turbulence intensity of approximately 0.5% [1].

3-1 Prolate Spheroid Model
The model was designed for measurements of surface pressure, boundary layer state, force and flow visualisation. A single row of tappings running from the front to the rear of the model allows the surface pressure to be measured. This row of tappings may be rotated to azimuthal angles, ψ, between 0° and 360° in 15° increments. The angle of incidence, α, of the spheroid may be altered between ±10° in 2° increments by switching an internal support. At 0° incidence the major axis of the prolate spheroid model is aligned in the

streamwise direction. A grid was placed on the model to facilitate the analysis of the flow visualisation measurements. The surface pressure and flow visualization are used in conjunction with the boundary layer survey to provide a more extensive understanding of the flow than is possible from any one of these techniques in isolation. An exploded image and a photo of the spheroid model are shown in Figure 1 and Figure 2 respectively. The model has a nominal length L of 330 mm but 4 mm is truncated from the rear in order to provide access for the sting support. The coordinates for the model are shown in Figure 3.

3D Traverse System

The three-dimensional automated traverse has interchangeable probe supports and is capable of operating over the full pressure range of the tunnel. The traverse is based on a 46 mm thick stainless steel plate that may be placed in any of the six side window frames of the tunnel test section, shown in Figure 4. The main traverse window has a square 225 mm opening that allows access for the probe. The probe is held in position by the traversing plate. This plate can slide ±100 mm vertically from the centre line of the tunnel on two sets of linear bearings. The rails that allow the plate to move vertically are indirectly attached to another set of linear bearings that allow the traversing plate to move ±100 mm horizontally from the centre of the window. An o-ring around the edge of the 225 mm opening provides a seal between the two plates. The traversing plate is large enough so that the o-ring around the opening in the main plate is always covered.

The traversing plate is sandwiched between the main traverse window and a 100 mm thick steel support frame designed to minimise the deflection of the traversing plate and the main traverse window when the tunnel is pressurised. The traversing plate consists of a central stainless-steel plate with Teflon adhered to both sides. The area of Teflon contacting the steel support frame is optimised to reduce friction as the traversing window/support frame interface is subjected to approximately four times the loading of the traversing window/main traverse window interface when the tunnel is at its maximum and minimum pressures respectively. The optimisation of the contact area of the Teflon ensured that at maximum tunnel pressure the pressure on the Teflon is approximately 3 N/mm^2, below this pressure the coefficient of friction for Teflon increases significantly. A series of thin plates on the inside of the traverse keep the flow around the traversing mechanism streamline (see Figure 5). The third axis allows the probe to be driven up to 300 mm perpendicular to the traversing plate. A hydrofoil-section support is used to minimise probe vibration when the probe is inserted more than 150 mm from the side of the tunnel.

The traverse is controlled by a closed loop system. Movement of the vertical and horizontal axes of the traverse is achieved using Frame-34 stepper motors and fine pitched roller screws. The fine-pitch roller screws allow these axes to be positioned accurately and with sufficient force to move the traverse when the tunnel is fully pressurised. A smaller Frame-17 stepper motor drives the probe attached to the traversing window. Linear position transducers measure the position of all axes. These measurements are read by the controller and used to move the axes until the desired position is reached. The resolution of the traverse in all axes is 0.02 mm, with an accuracy of better than 0.1 mm under most conditions. A remote control for the traverse has been developed to allow points on the surface of the model to be measured efficiently. These points are used to determine the position of the model in traverse coordinates.

Fast Response Probe

The Fast Response Probe (FRP) measures the total head with a miniature pressure sensor close to the tip. Placing the sensor close to the tip increases the measured bandwidth of the probe. This probe is similar to those used in transonic [2] and combusting [3] flow

applications. The FRP is illustrated in Figure 6. As can be seen in Figure 6 the FRP has been designed to be modular. It consists of three sections, a probe head, a sensor housing and a support stem. Each section can be changed to suit the flow being measured. The performance of the probe with a 1.2 mm tip and 3.5 bar sensor is detailed in Brandner et al [4]. For the measurements around the spheroid at an incidence of 10.2° degrees a 1.0 mm tip was used. For the subsequent tests at 0.2° and 6.2° a 0.6 mm tip was developed. The probe was otherwise as detailed in Brandner et al. [4] and uses a commercial miniature differential pressure transducer that operates by measuring the strain on a thin diaphragm. The transducer is referenced to the static pressure at the start of the test section, where the model has minimal influence on the freestream velocity, by means of a diaphragm. The diaphragm prevents moisture from the tunnel affecting the reference pressure side of the transducer. The boundary layer thickness at the centre of the model is comparable to the diameter of the probe tip.
The output of the probe has a natural frequency that is a function of the tube dimensions and the stiffness of the probe sensor. The resonance peak due to this natural frequency is filtered as shown in Figure 7.

Determining Model Position

The position of the model in traverse coordinates is determined by touching the model at a number of locations with the pitot probe and recording these points. If it is assumed that the surface of the model can be described by a quadratic function, the points at which the probe touched the model must satisfy the following equation

$$Ax_t^2 + By_t^2 + Cz_t^2 + Dx_t y_t + Ex_t z_t + Fy_t z_t + Gx_t + Hy_t + Iz_t = 1 \qquad (1)$$

where x_t, y_t, z_t are the traverse coordinate and $A \rightarrow I$ are the unknowns. As long as nine or more points on the surface of the body are available it is possible to determine the unknowns and thus the offset, rotation and size of the ellipsoid. Results determined for the unknowns using this solution were sensitive to error in the measurement of the points. This sensitivity is due to Eq.1 also being the equation for a number of different surfaces. A failing in this approach is that it does not use all the information that is available, i.e. that the shape is an ellipsoid with axes of known length (a, b, c). The equation of an ellipsoid with its axes aligned to the Cartesian coordinates x_{bc}, y_{bc}, z_{bc} with an offset (x_0, y_0, z_0) is given by

$$(x_{bc} - x_0)^2 / a^2 + (y_{bc} - y_0)^2 / b^2 + (z_{bc} - z_0)^2 / c^2 = 1. \qquad (2)$$

Rotating this by (ϕ, θ, ψ) about (z_t, y_t, x_t) respectively provides an equation for the surface of an ellipsoid with known major and minor axes. In order to determine the model's position in traverse coordinates the rotation (ϕ, θ, ψ) and offset (x_0, y_0, z_0) need to be determined. The non-linear equation obtained from the rotation of Eq.2, together with at least six points on the surface of the ellipsoid, may be used to determine the unknowns. The non-linear Levenberg-Marquardt minimisation routine in LabView was modified to handle more than one independent variable to perform the minimisation. In practice about twenty widely spaced points on the surface were measured in order to obtain positioning of the surface to within 0.1 mm. For the spheroidal model there is no requirement to solve for the rotation about the x axis.

Boundary Layer State

The boundary layer is initially laminar at the forward stagnation point. As it moves downstream it may become turbulent. The transition from laminar to turbulent boundary layer flow is described by Emmons [5]. The turbulent boundary layer is characterised by rapid fluctuations in velocity and pressure due to the eddying motion. The start of

transition is characterised by short turbulent bursts with rapid velocity and pressure fluctuations. As measurements are taken further downstream the duration and frequency of the turbulent bursts increase until the boundary layer is fully turbulent.

Hot films may be placed on the model surface [6] or pressure sensors may be placed flush with the surface or behind pinhole tappings in order to measure the fluctuations due to turbulence [7]. These two methods have the advantage that they are essential non-intrusive and can perform simultaneous measurements. A disadvantage is that they but do not give useful information in regions of separated flow. Each measurement point requires its own transducer and signal conditioning equipment. Hot wire, hot film and pressure probes may be traversed along the surface. These techniques allow for a high density of measurement points. However there are errors associated with intrusive nature of a probe. Regardless of the sensor a procedure is required to discriminate between periods of laminar and turbulent flow, Hedley and Keffer [8] together with Canepa [9] provide reviews on a number of these techniques. The output of these procedures is the instantaneous intermittency function, γ, which has a value of 1 when the boundary layer is turbulent and 0 when laminar.

For the tests reported in this paper the Peak-Valley Counting (PVC) algorithm [10] was selected, using $(\partial V/\partial t)^2$ as the detector function, where V was the output of the FRP total pressure signal. The PVC algorithm determines that a peak or valley has been found when the local maxima or minima exceed a threshold S. If another peak or valley occurs within the time window, T_w, the boundary layer is regarded as turbulent for the period between when the threshold was first exceeded and this subsequent peak, accordingly γ is set to 1 for this period. The starting point of the window is brought forward to this next peak and the process is repeated until no peak or valley occurs within the window T_w. On the final peak or valley the turbulent burst is considered to end when the detector function no longer exceeds the threshold. The amplitude of the threshold S and period of time window T_w used with this algorithm were determined experimentally. The threshold amplitude varied between 60 V^2/s^2 at a Reynolds Number of 1.0×10^6 to 1200 V^2/s^2 at a Reynolds Number of 4.0×10^6. A time window of 800 to 500 μs was used for Reynolds Numbers between 1.0×10^6 and 4.0×10^6. The example of the output of the FRP, detector function and PVC algorithm are shown in Figure 8 for the spheroid at a 6.2° incidence at an azimuth angle of $\psi = -105°$ for three chordwise positions at a Reynolds Number of 3.0×10^6.

RESULTS AND DISCUSSION

The FRP was used to survey the state of the spheroid's boundary layer for four Reynolds Numbers at each of three angles of incidence, 0.2°, 6.2° and 10.2°. The four Reynolds Numbers of 1.0, 2.0, 3.0 and 4.0×10^6 at a typical water temperature of 20°C corresponded approximately to velocities of 3, 6, 9 and 12 ms^{-1} respectively. The Reynolds number used the length of the model as the reference length. Surveys were taken every 15° for ψ between 0° and –180°. At $\psi = -90°$ the probe approaches normal to the surface; but as the probe is moved towards $\psi = 0°$ or $\psi = -180°$ the probe approaches the surface at a decreasing angle and is thus more likely to disturb the flow. For this reason the measurements at ψ = 0°, –15°, –165° and $-180°$ were not used. An estimate of the transition location at these angles was determined from perturbations in the mean surface pressure plots. This method is less reliable when there are large pressure gradients or the flow is complex.

Contours of the mean intermittency function, $\bar{\gamma}$, determined from the boundary layer survey are presented in Figures 9 – 12. Figures 9, 11 and 12 show a delayed onset of

transition on the pressure side of the body where an extended region of favourable (negative) pressure gradient exists. Conversely on the suction side where an extended region of adverse pressure gradient exists the boundary layer transitions further upstream. The figure displaying the results for a Reynolds Number of 2.0×10^6 shows the pressure side boundary layer to transition near the front of the model. A similar result was not seen from the surface pressure readings. The spurious results for this particular boundary layer survey are probably due to a small piece of debris sticking to the front of the model. Although demineralised water is used in this facility and it is regularly filtered this contamination of the surface demonstrates the sensitivity of boundary layer development to minor disturbances. The values less than 0 in Figures 8-11 indicate regions of the body either not surveyed or not displayed due to the low angle between the probe and the surface as previously discussed.

The transition from laminar to turbulent boundary layer generally occurred over a short interval of around 20 mm, or less than 10% of the body length. The RMS of the probe output also provides a good indicator of the transition from laminar to turbulent boundary layer as it tends to have a maximum as the boundary layer transitions.

CONCLUSION

This work highlights the capability of the traverse in accurately positioning (within 0.1 mm) the probe and the FRP ability when combined with appropriate software to determine the state of the boundary layer. This data will be used in accessing the capability of CFD to determine the flow around bodies subject to transitional flow when the location of transition is known.

ACKNOWLEDGMENTS

The authors wish to acknowledge the contribution of: Mr John Xiberras in the detailed design of the spheroid and support foil, Mr Vinh Nguyen in the detailed design of the 3D Traverse, Mr Paul Cooper and Mr Paul Vella in the manufacture of the spheroid, support foil and traverse, Mr Robert Wrigley for onsite manufacture and fitting. The support of DSTO and AMC has also been vital.

REFERENCES

[1] www.amc.edu.au/facilities/cavitation.tunnel

[2] Biagioni, L. and d'Agostino, L., 1999, "Measurement of Energy Spectra in Weakly Compressible Turbulence", AIAA 99-3516 30th AIAA Fluid Dynamics Conference

[3] Bradshaw, P., 1971, "An Introduction to Turbulence and its Measurement", Pergamon Press.

[4] Brandner, P. A., Clarke, D. B. and Walker, G. J., 2004, "Development of a Fast Response Pressure Probe for Use in a Cavitation Tunnel", 15th Australasian Fluid Mechanics Conference

[5] Emmons H. W., 1951, "The Laminar-Turbulent Transition in a Boundary Layer – Part 1", Journal of the Aeronautical Sciences", Vol. 18, No 7, 490-498.

[6] Meier, H. U. and Kreplin, H. P., 1980, "Experiment Investigation of the Boundary Layer Transition and Separation on a Body of Revolution", Zeitschrift f. Flugwiss. Weltraumforsch., Vol. 4, 65

[7] Bull M. K., 1996, "Wall-Pressure Fluctuations beneath Turbulent Boundary Layers: Some Reflections on Forty Years of Research", Journal of Sound and Vibration, 190(3), 299-315.

[8] Headley T. B. and Keffer J. F., 1974, "Turbulent/non-turbulent decisions in an intermittent flow", J. Fluid Mech. Vol. 64, part 4, 625-644.

[9] Canepa E., “Experiences in the application of intermittency detection techniques to hot-film signals in transitional boundary layers”, The 16th Symposium on Measuring Techniques in Transonic and Supersonic Flow in Cascades and Turbomachines.
[10] Solomon, W. J., 1996, “Unsteady boundary layer transition on axial compressor blades”, Ph.D. thesis, University of Tasmania.

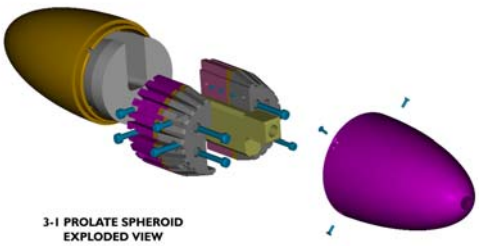

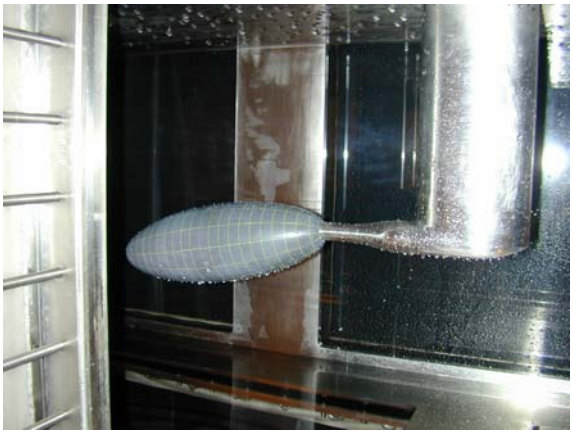

Figure 1: Exploded View of 3-1 Spheroid Model for AMC Cavitation Tunnel (left)

Figure 2: 3-1 Spheroid sting mounted in AMC Cavitation Tunnel test section (right)

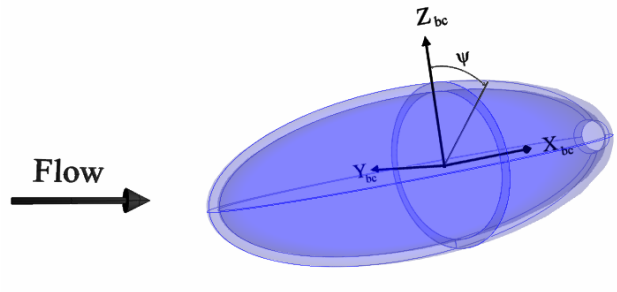

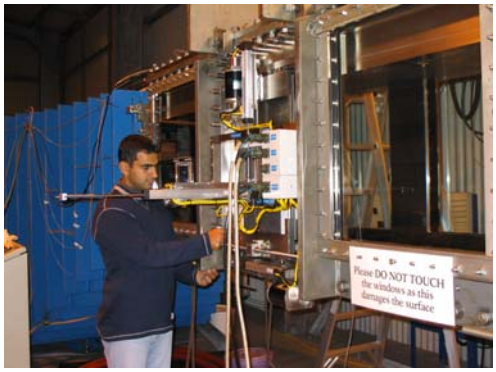

Figure 3: Coordinates for 3-1 spheroid model (left)

Figure 4: Traverse mounted in centre window of tunnel test section (right)

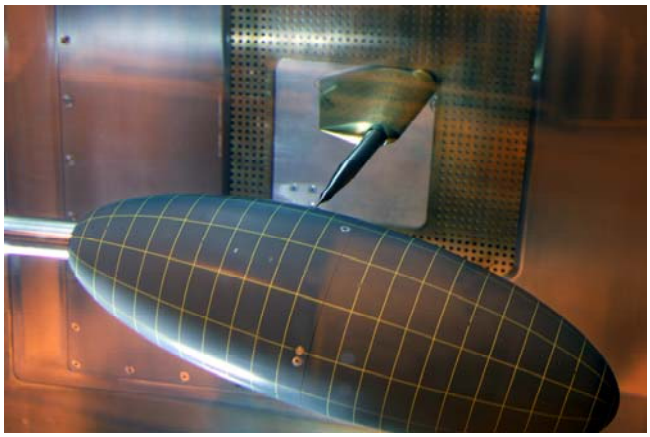

Figure 5: Traverse Interior

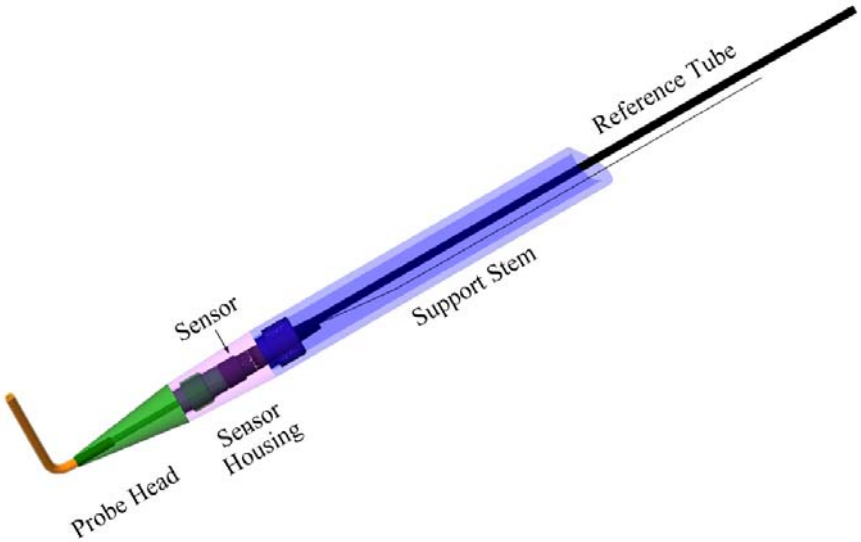

Figure 6: Fast Response Probe

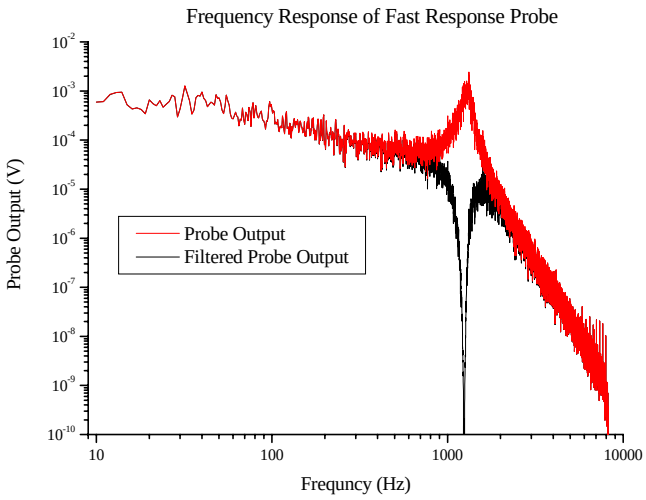

Figure 7: Frequence Response of FRP with 0.7 mm tip

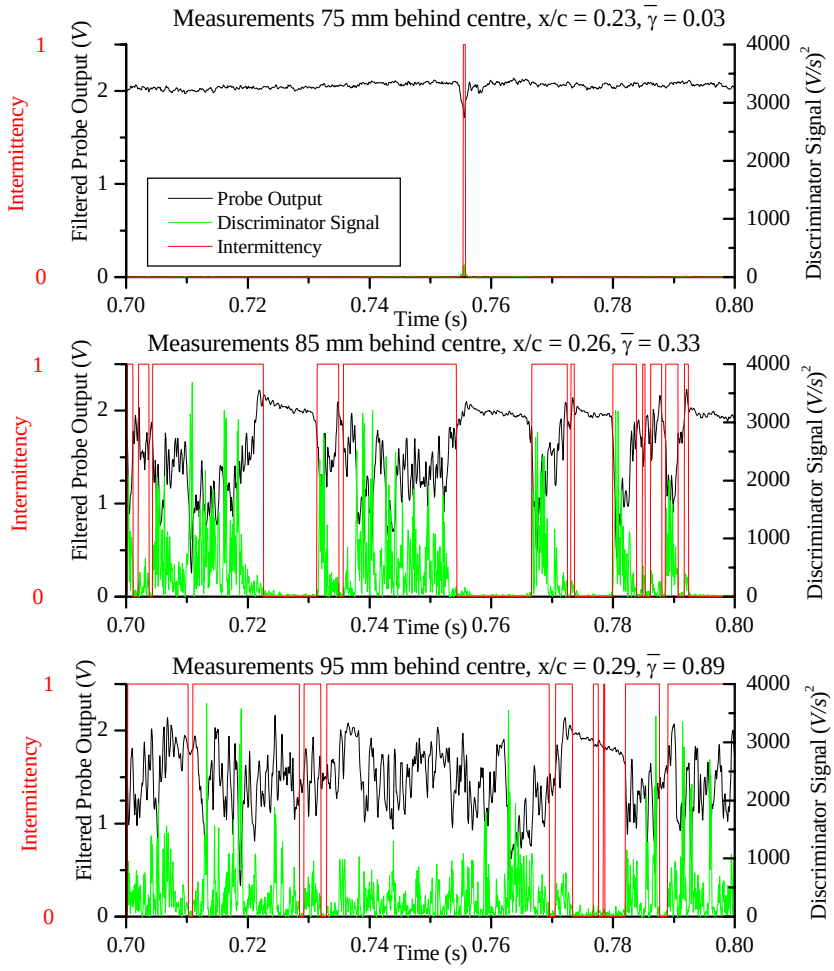

Figure 8: Intermittency measurements on spheroid

Intermittency Measurements on 3-1 Spheroid at 10.2° Incidence
Re = 1.0 ×10 ^{6}

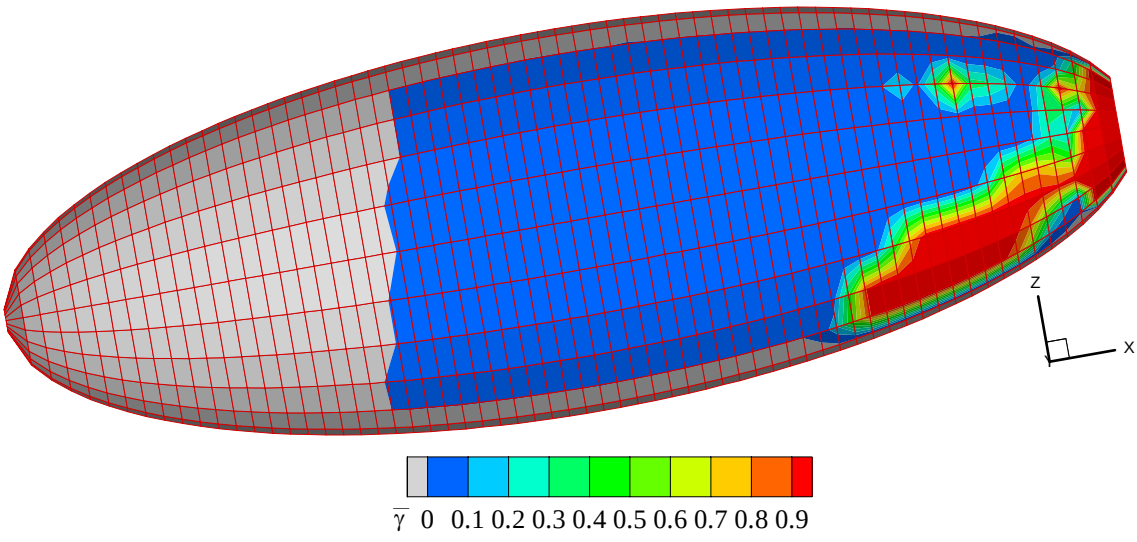

Figure 9: Boundary layer survey on Spheroid at Re = 1.0×10^6, α =10° degree

Intermittency Measurements on 3-1 Spheroid at 10.2° Incidence
Re = 2.0 ×10 6

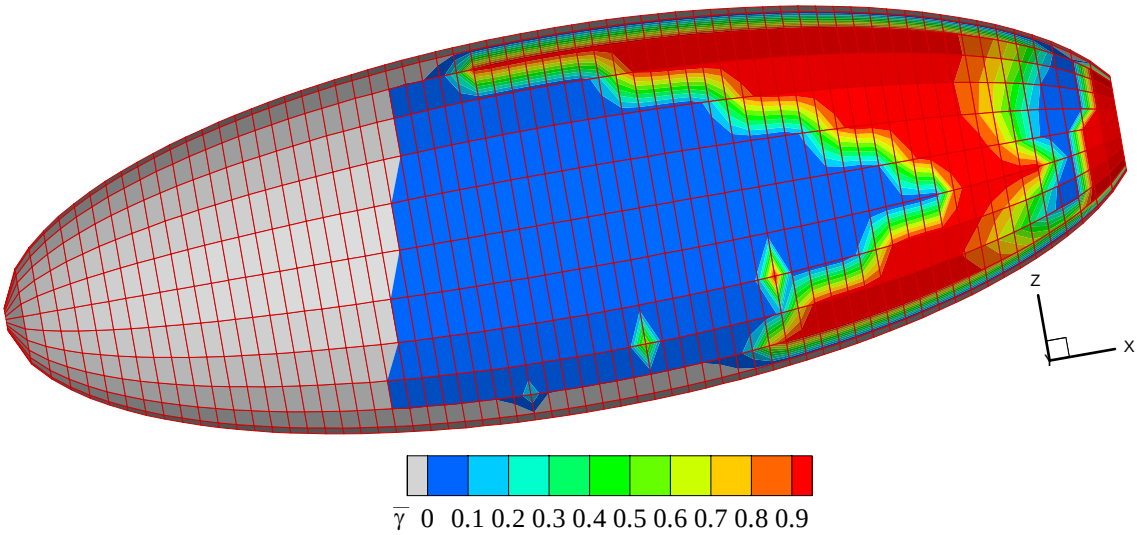

Figure 10: Boundary layer survey on Spheroid at Re = 2.0×10^6, α =10° degree

Intermittency Measurements on 3-1 Spheroid at 10.2° Incidence
Re = 3.0 ×10 6

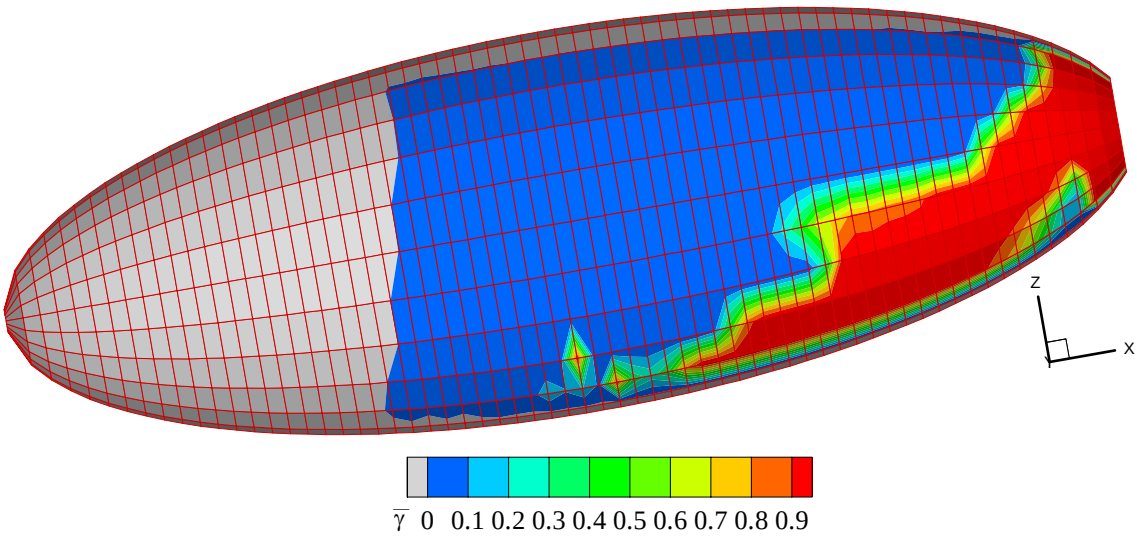

Figure 11: Boundary layer survey on Spheroid at Re = 3.0×10^6, α =10° degree

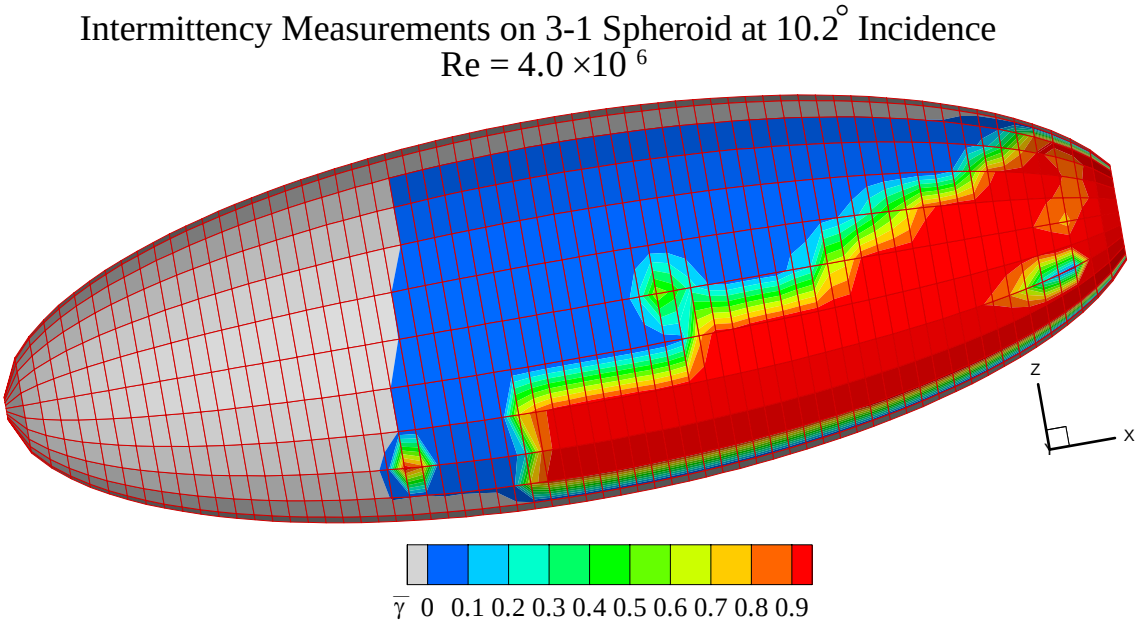

Figure 12: Boundary layer survey on Spheroid at Re = 4.0×10^6, α =10° degree